Scientific Research Publishing

Optics and Photonics Journal, 2022, 12, 253-268
https://www.scirp.org/journal/opj
ISSN Online: 2160-889X
ISSN Print: 2160-8881

Super-Resolution Stress Imaging for Terahertz-Elastic Based on SRCNN

Delin Liu[1], Zhen Zhen[1], Yufen Du[2], Kai Kang[2], Haonan Zhao[2], Chuanwei Li[2], Zhiyong Wang[2*]

[1]Aviation Key Laboratory of Science and Technology on Advanced Corrosion and Protection for Aviation Material, Beijing Institute of Aeronautical Materials, Beijing, China
[2]Department of Mechanics, Tianjin University, Tianjin, China
Email: *zywang@tju.edu.cn

How to cite this paper: Liu, D.L., Zhen, Z., Du, Y.F., Kang, K., Zhao, H.N., Li, C.W. and Wang, Z.Y. (2022) Super-Resolution Stress Imaging for Terahertz-Elastic Based on SRCNN. *Optics and Photonics Journal*, **12**, 253-268.
https://doi.org/10.4236/opj.2022.1211019

Received: October 20, 2022
Accepted: November 25, 2022
Published: November 28, 2022

Abstract

Limited by diffraction limit, low spatial resolution is one of the shortcomings of terahertz imaging. Low spatial resolution is also one of the reasons limiting the development of stress measurement using terahertz imaging. In this paper, the full-field stress measurement using Terahertz Time Domain Spectroscopy (THz-TDS) is combined with Super-Resolution Convolutional Neural Network (SRCNN) algorithm to obtain stress fields with high spatial resolution. A modulation model from a plane stress state to a THz-TDS signal is constructed. A large number of simulated sets are obtained to train the SRCNN model. By applying the trained SRCNN model to imaging the numerical and physical stress fields, the improved spatial resolution of stress field calculated from the captured THz-TDS signal is obtained.

Keywords

THz-TDS, Stress Measurement, Super-Resolution Convolutional Neural Network

1. Introduction

Terahertz technology has obtained great development in recent 20 years [1] [2]. It has great application prospects in nondestructive testing, biomedical imaging, safety inspection and astronomy science [3] [4] [5] [6]. In terms of mechanics, it is possible to measure the internal stress of optically opaque materials [7] [8].

Based on the stress-optic effect of materials in the THz band, the THz-TDS technique can be used to measure the internal stress of optically opaque materials. In 2008, Ebara [9] *et al.* measured the stress-induced birefringence of several opaque polymers using a THz-TDS system. In 2011, Takahashi [10] *et al.*

obtained an intensity image of THz radiation on a loaded polyethylene specimen, and detected internal cavity interfaces and mechanical stresses. Since 2014, Li, Wang [11] [12] *et al.* have proved the validity of stress optical law in THz band. Three plane stress state parameters of isotropic and anisotropic materials were measured by using a polarization-sensitive THz-TDS system. The full-field two-dimensional stress state of the stressed specimen can be obtained by point-by-point scanning in the THz-TDS system. However, the low spatial resolution of THz radiation and the limited scanning step size limit the resolution and quality of THz stress imaging. Therefore, it is worth studying to improve the spatial resolution of THz stress measurement.

Using a super resolution algorithm based on interpolation, reconstruction or deep learning to process the obtained low resolution image data can effectively improve their spatial resolution. In 2014, Dong [13] *et al.* proposed a Super-Resolution Convolutional Neural Network (SRCNN) algorithm, which is based on deep convolutional neural network (CNN) learning. The algorithm established the end-to-end mapping function between high- and low-resolution images, to achieve a better reconstruction quality for low-resolution images. Inspired by this classic work, some powerful machine learning algorithms were developed [14] [15] [16]. But these algorithms have great limitations when applied directly to THz images due to their particularity.

Low resolution is one of the major shortcomings of THz imaging. In 2019, Long [17] *et al.* analyzed the degradation model of THz images and designed a deep CNN model with super resolution ability for THz images. In 2020, Li [18] *et al.* proposed a three-dimensional degradation model for the imaging process of real aperture scanning, taking into account the focus beam distribution and accurate ranging capability of the general THz system. They introduced an adjustable CNN, which produces an improved resolution by simply adjusting the input coefficients. The above work only used the intensity information of THz image. In 2021, Lu [19] *et al.* have proposed a mathematical degradation model of THz images by considering blur, noise, and low sampling resolution. Recently, Ljubenovic [20] [21] *et al.* developed an effective algorithm to reduce the effects of degradation from frequency-dependent blur and noise. These works have improved the image quality from THz radiation. However, these developed algorithms are not suitable for THz stress imaging. This is because these algorithms are based on the amplitude of THz signal, but the stress field will modulate the amplitude and phase of THz signal simultaneously.

In this paper, we developed a super resolution algorithm specialized for stress imaging using THz-TDS to improve its resolution and quality. The rest of this paper is organized as follows. In Section 2, the modulation model from stress field to THz signal is established on the basis of the stress-optic effect. By the classic SRCNN algorithm, the end-to-end mapping of low resolution (LR) stress field to high resolution (HR) stress field is realized, and the CNN model of super resolution (SR) for LR stress field is trained. In Section 3, we perform two verification experiments to demonstrate the SR reconstruction abil-

ity of the trained CNN. In Section 4, some discussion and conclusive remarks are presented.

2. Data Simulation and Network Training

2.1. Data Simulation

To train the CNN model, a large amount of training data is normally needed. For example, Dong *et al.* uses 91 images as the training set in SRCNN [13]. However, the scanning imaging using THz-TDS is very time-consuming. In order to provide a large amount of training data for the CNN model, we use the key parameters of the used THz-TDS system to generate a large number of simulated THz-TDS images. Here, the used key parameters included the diameter of THz spot and the noise level of the used THz-TDS system. Figure 1 shows the flow of data processing in this work.

In this work, our aim is to obtain high resolution plane stress fields. The stress state at a point contains three stress components, σ_x, σ_y and τ_{xy}. These stress components are not independent, and should satisfy the following balance equation,

$$\begin{aligned} \frac{\partial \sigma_x}{\partial x} + \frac{\partial \tau_{yx}}{\partial y} = 0 \\ \frac{\partial \tau_{xy}}{\partial x} + \frac{\partial \sigma_y}{\partial y} = 0 \end{aligned} \tag{1}$$

We supply 30 different stress fields as the training sets, and another 5 stress fields are used as the test set. These training and test data contain different forms of stress distribution function.

Figure 2 presents optical setup of the used THz-TDS system. The THz-TDS system used a commercial THz time domain spectrometer (Terahertz photonics Co. Ltd. TPF15K). The THz radiation is generated and detected by two rotatable photoconductive antennas. The emitting antenna generates the polarized THz radiation, and the polarization direction can be adjusted by rotating the antenna. In the implementation process, we carried out data simulation and experimental measurement in the dark field. The dark field here refers to the configuration, in

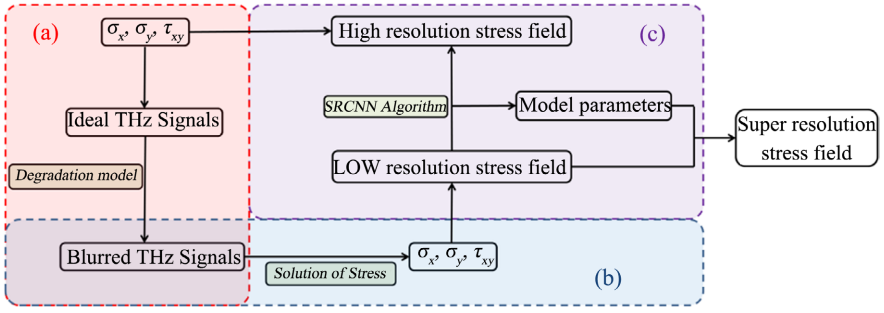

Figure 1. The flow of data processing (a) Data simulation; (b) Solution of stress; (c) CNN training.

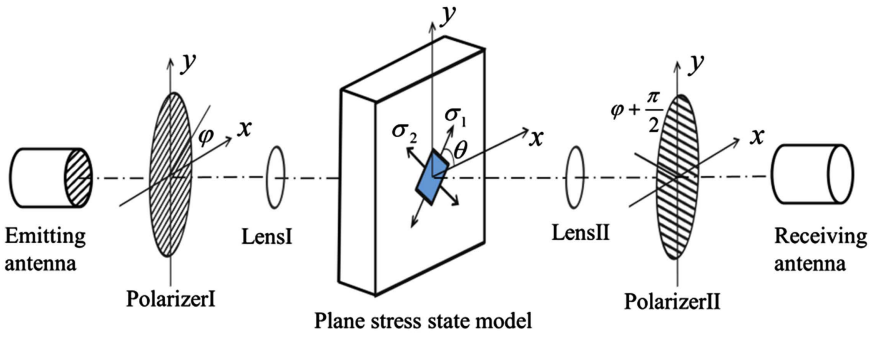

Figure 2. Stress measurement system based on terahertz time domain signal under dark field.

which the polarization direction of the emitting antenna is perpendicular to that of the receiving antenna. The angle between the polarization direction of emitting antenna and the horizontal direction is φ, and the angle between the polarization direction of receiving antenna and the horizontal direction is $\varphi + \pi/2$. That is, the THz signal strength passing through the unstressed specimen under ideal conditions is zero (complete extinction). To obtain the high extinction rate, two polarizers are used in this system as shown in **Figure 2**. Their polarization directions are set to be consistent with those of the emitting and receiving antenna, respectively. In **Figure 2**, the lens is used to focus THz radiation on the specimen. After focusing, the diameter of the spot is about 5.5 mm, which is measured by the traditional blade method. The highly reliable frequency range of the used system was during 0.2 - 2.5 THz. For subsequent convenience, the horizontal direction will be referred as x-axis, and the vertical direction as y-axis.

As the THz radiation passes through the specimen under test, only part of it can get through the air-sample and sample-air interface. The classic Fresnel formula is used to calculate the transmission coefficient,

$$t_{ab} = \frac{2N_a}{N_a + N_b}, t_{ba} = \frac{2N_b}{N_b + N_a}, \tag{2}$$

where $N_a = 1$ is the refractive index of air, N_b is the refractive index of the specimen, t_{ab} and t_{ba} represent the transmission coefficients at air-sample and sample-air interface, respectively.

According to the material mechanics, the principal stress σ_1, σ_2 and principal stress direction θ of a plane stress state can be calculated from σ_x, σ_y and τ_{xy} by

$$\begin{aligned} \left.\begin{matrix}\sigma_1 \\ \sigma_2\end{matrix}\right\} &= \frac{\sigma_x + \sigma_y}{2} \pm \sqrt{\left(\frac{\sigma_x - \sigma_y}{2}\right)^2 + \tau_{xy}} \\ \theta &= 0.5 \arctan\left(\frac{-2\tau_{xy}}{\sigma_x - \sigma_y}\right) \end{aligned}. \tag{3}$$

According to the stress optic law, when a plane polarized beam is incident vertically on a specimen under plane stress state, it is divided into two polarized components along the two principal stress directions. The propagation velocities

of the two plane-polarized beams are different in the specimen. This causes the material to behave as optical anisotropy, resulting in birefringence. The relation between principal stress and refractive index is expressed as

$$\begin{aligned} N_1 - N_0 &= A\sigma_1 + B\sigma_2 \\ N_2 - N_0 &= A\sigma_2 + B\sigma_1 \end{aligned}, \tag{4}$$

where N_0 represents the initial refractive index in the stress-free state, N_1 and N_2 are the refractive index along the directions of σ_1 and σ_2, and the stress optic coefficients $A = 2.03 \times 10^{-9}$, $B = 2.63 \times 10^{-9}$ [11] for the material to be used in the subsequent experiments, Poly Tetra Fluoro Ethylene (PTFE). It should be noted that Equation (4) is valid only when the stress is less than the elastic limit of material.

When the two beams of plane polarized light pass through the specimen and reach the second polarizer, the two beams are combined on its polarization direction. Finally, the THz signal is detected through the receiving antenna. If the amplitude and phase of the received THz signal through stress-free specimen are unit and zero, respectively, following a deduction procedure similar to that in Ref. [12], the signal received through specimen under plane stress state E can be expressed as

$$E = \sin 2(\theta - \varphi) \cdot \sin \frac{\delta_1 - \delta_2}{2} \cdot \mathrm{e}^{i\left(\frac{\pi}{2} + \delta_1 + \delta_2\right)} \tag{5}$$

where

$$\begin{aligned} \delta_1 &= \frac{2\pi f d}{c}\left(A\sigma_1 + B\sigma_2\right) \\ \delta_2 &= \frac{2\pi f d}{c}\left(A\sigma_2 + B\sigma_1\right) \end{aligned} \tag{6}$$

In Equation (6), δ_1 and δ_2 are the phase change of the THz radiations polarized along the direction of σ_1 and σ_2, respectively. Based on the above model in Equation (5), we can obtain a simulated ideal THz signal modulated by a plane stress state.

2.2. Degradation Model

The THz signal simulated in 2.1 is totally ideal. In the physical experiment, the captured THz images by step scanning method are degraded due to Gaussian blur, rough scanning step and random noise. A model here is proposed to reflect these degradation effects in the physical experiments.

Firstly, since the THz beams generally obey the Gaussian distribution and spot diameter has been measured, a Gaussian kernel function G in Equation (7) is adopted to simulate the effect of Gaussian blur.

$$G(x, y) = \frac{1}{2\pi m^2} \exp\left[-\frac{x^2 + y^2}{2m^2}\right], \tag{7}$$

where m is the standard deviation of the Gaussian kernel. After a scanning mapping, we get a three-dimensional THz image of $a \times b \times 1000$. Here, a and b

represent the width and height of the images, and 1000 is the signal length of the time-domain waveform at each point. In other words, we get 1000 two-dimensional images. Each image is called a layer. The spatial sampling spacing of the simulation field is 0.05 mm, which is the resolution we want to achieve. Then, the 0.05 mm-resolution images in each layer is blurred by the kernel in Equation (7). When using Equation (7), the value of m is key. The measured radius of THz spot is about 5.5 mm. We estimate 95% of the energy of the spot is concentrated in the area with a diameter of 5.5 mm. In order to consider possible randomness of spot diameter in practice, the standard deviation m takes random values in the range of 1 mm - 1.5 mm in the simulation processing.

Secondly, the step of the scanning imaging is one of the key factors affecting the resolution. In physical experiment, it will take about 40 hours to scan a 50 mm × 50 mm area with a step size of 0.5 mm by our used system, so it is not practical to carry out many experiments with a smaller step. So after Gaussian blurring, each layer with a resolution of 0.05 mmis down sampled to one tenth of the original size to simulate the effect of the limited size of scanning step. This method has also been used in the classic literature of SRCNN to simulate the limited spatial resolution in the original images [13].

Finally, the electromagnetic random noise is inevitable in the used THz-TDS system. Thus, we capture several THz signals through air, and then estimate the level of random noise. At last, each layer is added by a Gaussian random noise with a mean of 0, and standard variance of α. The standard variance is determined by the physically captured signal of dark field configuration, in which the ideal signal should be zero. Ten signals are collected to evaluate the noise level, and finally α take one percent of the maximum signal intensity.

In order to include the above three degradation factors, a degradation model in Equation (8) is adopted.

$$L = (H \otimes G) D_s + n, \tag{8}$$

where H is the ideal THz signal, L is the degraded THz signal, G represents the Gaussian blurred kernel, $\otimes$ represents the convolution operation, D_s is a sub-sampler, and n is the additive noise with a noise level of α. Considering that THz waves may produce different levels of noise in practice, multiple levels of noise should be taken into the training set. The degraded THz signal from Equation (8) is considered to be a simulation of a physically experimental signal.

By combing the Fresnel model in Equation (2), the stress optic effect in Equation (4), and the degradation model in Equation (8), we can get a large number of simulated experimental THz signals through a plane-stressed specimen for training the neural network.

2.3. Calculation of Stress Fields

In 2.1, an original stress field is supposed, and it is used to produce an ideal signal. In 2.2, we simulate the degenerated terahertz images. In this part, we need to calculate the stress field from the degenerated images. In this way, the original and

calculated stress fields, which respectively represent the high- and low-resolution images, compose a pair of learning data.

The stress field can be calculated from the captured THz signals at the two polarization configurations of $\varphi = 0$ and $\varphi = \pi/4$. According to Equation (5), the principal stress difference $\sigma_1 - \sigma_2$, the principal stress sum $\sigma_1 + \sigma_2$ and the principal stress direction θ can be calculated as

$$\begin{aligned}
\sigma_1 - \sigma_2 &= -\frac{c}{\pi f d\left(A-B\right)} \arcsin \frac{\left\|E\right\|_{\varphi=\pi/4}}{\cos 2\theta} \\
\sigma_1 + \sigma_2 &= \frac{c}{\pi f d\left(A+B\right)} \left(\frac{\delta_{\varphi=0} - \delta_{\varphi=\pi/4}}{2} + \frac{\pi}{2} \right) \\
\theta &= -\frac{1}{2} \arctan \frac{\left\|E\right\|_{\varphi=0}}{\left\|E\right\|_{\varphi=\pi/4}}
\end{aligned} \tag{9}$$

In Equation (9), $||E||_{\varphi=0}$ and $||E||_{\varphi=\pi/4}$ are the amplitude of the received radiation when the polarization angle $\varphi = 0$ and $\varphi = \pi/4$. As indicated in Equation (9), we can obtain a set of $\sigma_1 - \sigma_2$, $\sigma_1 + \sigma_2$, and θ from each frequency. In the work, the average value at different frequencies is used as their measurement results.

2.4. Training Model

The neural network form adopted in this paper is similar to SRCNN in Ref. [13]. Instead of training the gray value of the image or the Y channel in the YCbCr channels, this paper realizes the end-to-end training from low-resolution stress field to high resolution stress field. As indicated in **Figure 3**, the mapping of low-resolution stress field σ_L to high resolution stress field σ_H is realized by three layers convolution operation. These three convolution operations are Patch Extraction and Representation, Non-linear Mapping and Reconstruction, as proposed in Ref. [13]. We will detail these three layers in turn.

Feature Extraction: This operation extracts (overlapping) patches from the stress field σ_L of three channels with low resolution, and represents each patch as a n_1-dimensional vector.

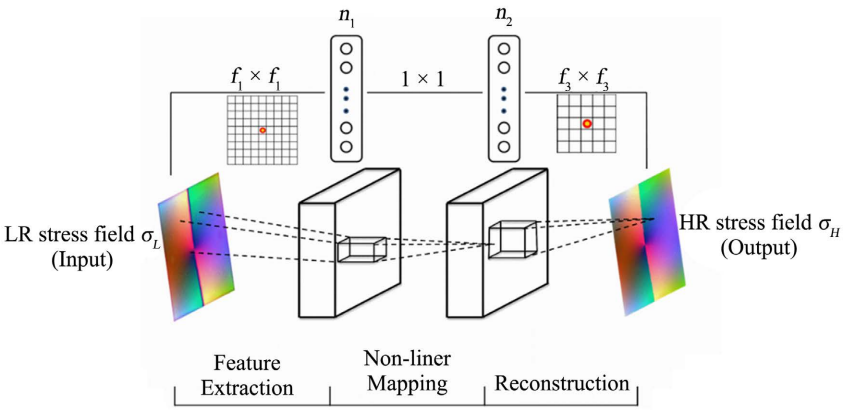

Figure 3. The used network of terahertz super resolution stress field measurement based on convolutional neural network.

$$F_1(\sigma_L) = \max(0, W_1 \otimes \sigma_L + B_1), \tag{10}$$

where W_1 and B_1 represent the filters and biases, respectively. Here W_1 is of a size $3 \times f_1 \times f_1 \times n_1$, and B_1 is an n_1-dimensional vector.

Non-linear mapping: this operation nonlinearly maps each n_1-dimensional vector onto another n_2-dimensional vector by the following Equation (7). Each mapped vector is conceptually the representation of a high resolution patch.

$$F_2(\sigma_L) = \max(0, W_2 \otimes F_1(\sigma)_L + B_2), \tag{11}$$

where W_2 is of a size $n_1 \times 1 \times 1 \times n_2$, and B_2 is n_2-dimensional.

Reconstruction: This operation aggregates the above n_2-dimensional patchwork representations to produce the final high resolution stress field using

$$F(\sigma_L) = W_3 \otimes F_2(\sigma_L) + B_3, \tag{12}$$

where W_3 is of a size $n_2 \times f_3 \times f_3 \times 3$, and B_3 is a three-dimensional vector.

Learning the end-to-end mapping function F requires the estimation of parameters $\Theta = \{W_1, W_2, W_3, B_1, B_2, B_3\}$. The mean square error function shown in Equation (13) is used as the loss function to minimize the loss between the trained stress field $F(\sigma_L)$ and the real stress field σ_H.

$$L(\Theta) = \frac{1}{N}\sum_{i=1}^{N}\left\| F(\sigma_{Li}, \Theta) - \sigma_{Hi} \right\|^2, \tag{13}$$

where N is the total number of sub-field in the training process.

In the training phase, we set $f_1 = 9$, $f_3 = 5$, $n_1 = 64$ and $n_2 = 32$ in our implementation. The filter weights of each layer are initialized by drawing randomly from a Gaussian distribution with zero mean and standard deviation 0.001. The learning rate is 10^{-4} for the first two layers, and 10^{-5} for the last layer as suggested by Ref. [13].

In order to facilitate the display of the training set and test set, we transfer the normalized principal stress difference, principal stress sum and principal stress direction into RGB three color image channels respectively. Figure 4 presented a visual display of the training set and test set.

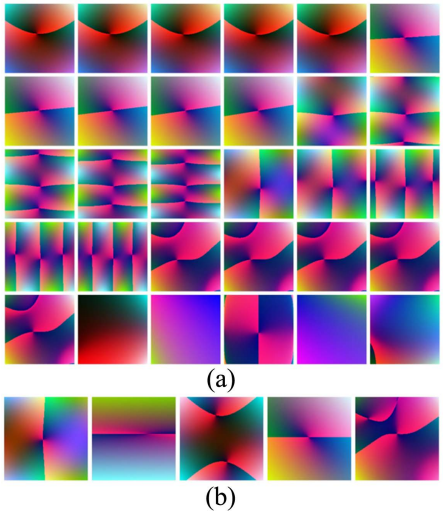

Figure 4. The visual display of the training set (a) and the test set (b).

We train the models in a Intel(R) Core(TM) i5-9400F CPU and NVIDIA GeForce RTX 2060 GPU with Caffe package [22].

3. Result

We train the convolutional neural network for all three channels simultaneously. The three channels are principal stress difference, principal stress sum, and principal stress direction. After one million rounds of back propagation training, the mean square error of the test set in Equation (13) is reduced to 0.09. Based on the trained neural network, two verification experiments are conducted. The first experiment is a numerical experiment, while the other is a physical experiment.

3.1. Numerical Experiment

In this numerical experiment, the stress field conforming to a function presented in Equation (14) is selected to demonstrate the super resolution ability of the trained neural network. The corresponding principal stress difference $\sigma_1 - \sigma_2$, principal stress sum $\sigma_1 + \sigma_2$ and principal stress direction θ can be calculated by using Equation (3).

$$\begin{aligned} \sigma_x &= 2\sin\left(\frac{x}{25}\right)+0.1 \\ \sigma_y &= -\frac{1}{625}y^2\sin\left(\frac{x}{25}\right)-0.2, \\ \tau_{xy} &= -\frac{2}{25}y\cos\left(\frac{x}{25}\right)+0.1 \end{aligned} \tag{14}$$

Figures 5-7 shows the super resolution effect of principal stress difference, principal stress sum, and principal stress direction, respectively. In these three figures, (a) sub-figures show the ideal high resolution fields obtained by Equation (14), (b) ones show the degraded low resolution fields simulated by the method in Section 2.1, and (c) ones show the super resolution fields obtained from the trained neural network. There is a sharp jump near $y = -5.5$ mm in Figure 7(a), which is an ideal position for us to observe the super resolution effect. In Figure 7(b), the jump become blurred and smooth due to Gaussian blur of large focus spot and random noise. In Figure 7(c), the jump is partially restored. Obviously, this jump in Figure 7(c) is sharper than that in Figure 7(b). This demonstrates the ability of the trained neural network to a certain extent. However, after all, the super-resolution of the network is limited, and it is impossible to recover all the details perfectly. For example, at the location of $x = 17$ mm, $y = -5.5$ mm in Figure 7(a), the field has sharp jump in both x and y directions. After super reconstruction, the horizontal change in the vicinity $x = 17$ mm along $y = -5.5$ mm line in Figure 7(c) is still more blurred than that in Figure 7(a).

In order to exhibit the super-resolution ability of the proposed algorithm in more detail, Figure 8 shows the stress components when $x = -25.5$ mm. In this figure, the solid line shows the ideal high resolution components, the spot line

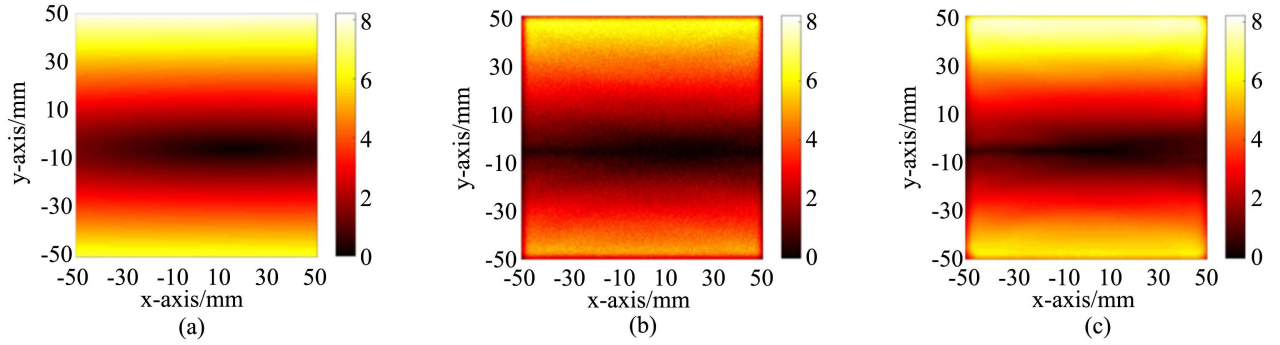

Figure 5. The result of principal stress difference (a) HR; (b) LR; (c) SR.

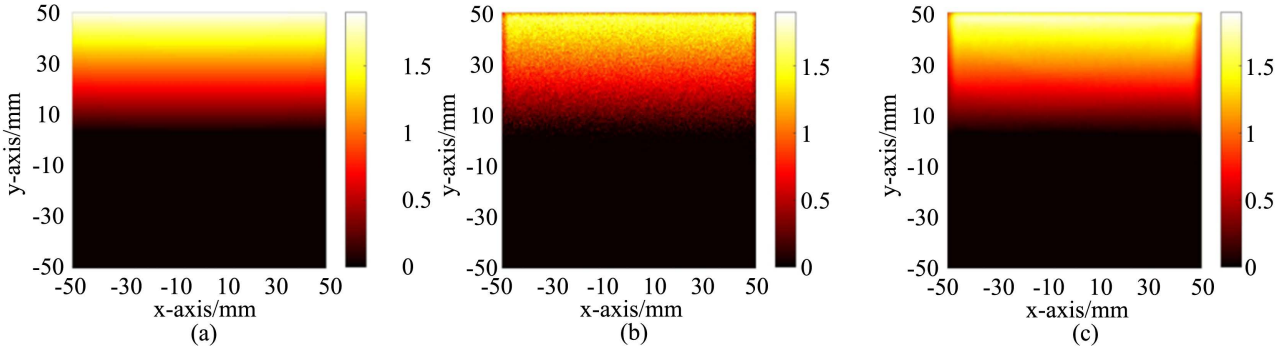

Figure 6. The result of principal stress sum (a) HR; (b) LR; (c) SR.

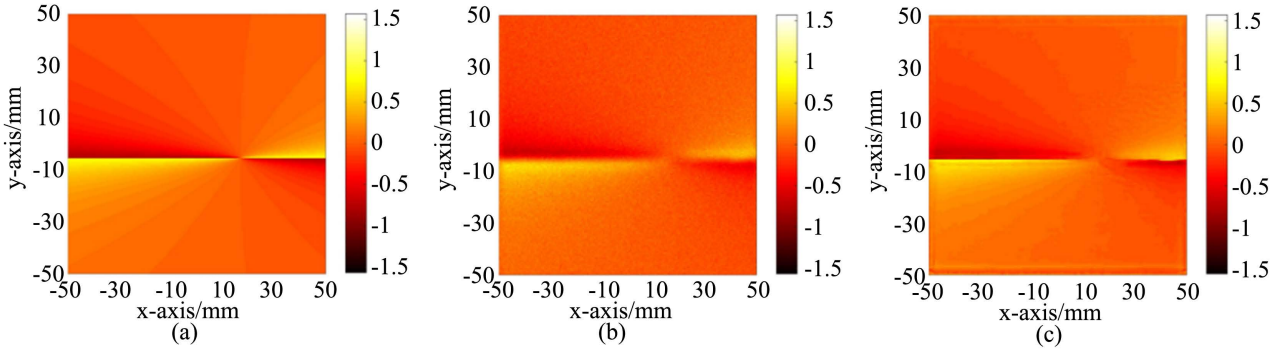

Figure 7. The result of the principal stress direction (a) HR; (b) LR; (c) SR.

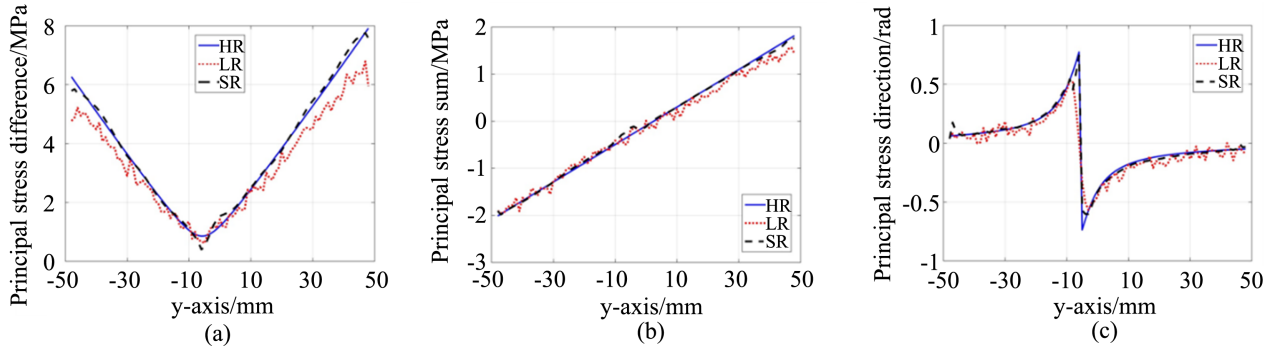

Figure 8. Stress comparison when $x = -25.5$ mm (a) the principal stress difference (b) the principal stress sum (c) the principal stress direction.

shows the blurred low resolution components simulated by the method in Section 2.1, and the dotted line shows the super resolution components obtained from the trained neural network. Obviously, the random variation of the simulated field (*i.e.* the spot line) is depressed in the super resolution result (*i.e.* the dotted line). So the trained neural network has the ability of depressed random noise. Figure 8(c) more intuitively shows the ability of the trained neural network to restore the sharp jump.

3.2. Physical Experiment

In this section, a diametrical loaded disk is chosen to demonstrate the ability of the proposed super resolution algorithm in physical experiment. Figure 9 shows the setup of the diametrical loaded disk experiment. The loading device is installed on a two-dimensional scanning platform to facilitate us to obtain two-dimensional terahertz spectral fields. In the experiment, a scanning step of 0.5 mm is adopted.

According to elastic mechanics theory, the analytical stress distribution of the loaded disk should be

$$\begin{cases} \sigma_x = \dfrac{2p}{\pi t}\left\{\dfrac{(r+y)x^2}{\left[(r+y)^2+x^2\right]^2}+\dfrac{(r-y)x^2}{\left[(r-y)^2+x^2\right]^2}-\dfrac{1}{2r}\right\} \\ \sigma_y = \dfrac{2p}{\pi t}\left\{\dfrac{(r+y)^3}{\left[(r+y)^2+x^2\right]^2}+\dfrac{(r-y)^3}{\left[(r-y)^2+x^2\right]^2}-\dfrac{1}{2r}\right\} \\ \tau_{xy} = \dfrac{2p}{\pi t}\left\{\dfrac{(r+y)^2 x}{\left[(r+y)^2+x^2\right]^2}-\dfrac{(r-y)^2 x}{\left[(r-y)^2+x^2\right]^2}\right\} \end{cases}, \tag{15}$$

where p is the applied force, r and t are the radius and the thickness of the disk, and x, y is the coordinate in space. The corresponding principal stress difference $\sigma_1 - \sigma_2$, principal stress sum $\sigma_1 + \sigma_2$ and principal stress direction θ can be calculated by using Equation (3). In this experiment, the disk material is PTFE. The experimental parameters are presented in Table 1.

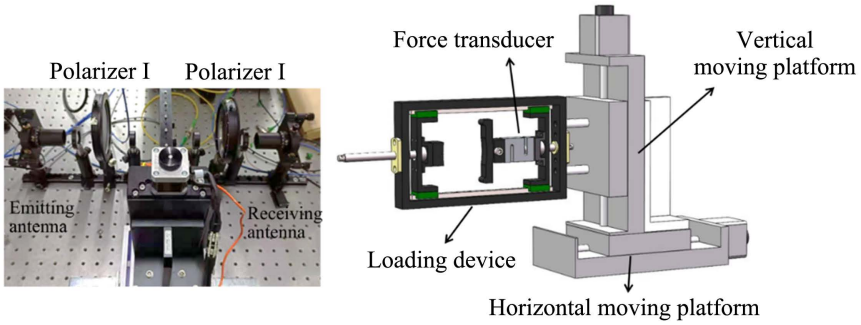

Figure 9. The schematic of the diametrical loaded disk (a) the experimental device; (b) two-dimensional moving platform.

Table 1. The key parameters in the experiment.

Material	Thickness	Radius	Loading	Scanning Step	A	B
PTFE	10 mm	25 mm	1000 N	0.5 mm	2.03×10^{-9} Pa^{-1}	2.63×10^{-9} Pa^{-1}

Figure 10 presented the high resolution stress field distribution from Equation (15). Figure 11 shows the low-resolution stress fields from the actual THz signal by Equation (9). In Figure 10(a), there are two approximately circular bright spots near the loading points. In Figure 10(b), there are two dark spots. By comparison, in Figure 11(a) and Figure 11(b), it is found that the bright and dark spots in the low resolution field become blurred, and their boundaries become smooth. Furthermore, comparing Figure 10(c) and Figure 11(c), we can find that the mutation in the θ field near the loading points in the low-resolution fields is blurred. These should be caused by large terahertz Gaussian spot, inevitable random noise and limited scanning step.

In order to restore more details of the stress fields, the trained network is adopted to obtain its super resolution counterpart. Figure 12 shows the super resolution stress fields. In order to show the super resolution effect in more detail, Figure 13 shows the principal stress difference when $y = 0$ mm and the principal stress direction when $x = 12.5$ mm, respectively. After super resolution network processing, the boundary of bright and dark spots in the Figure 12(a) and Figure 12(b) become sharper than that in Figure 11(a) and Figure 11(b). The edge of angle mutation in the Figure 12(c) also becomes clear. Figure 13 demonstrates the noise depression capability of the used neural network. Furthermore, it is obvious the super resolution results are closer to the analytical solution in Figure 13.

In order to quantify the effect of the trained neural network, error analysis is performed on simulated data and experimental data. The mean square error of principal stress difference, principal stress sum, and principal stress direction are calculated respectively. The mean square error here refers to the average relative error of the LR result and the SR result with respect to the analytical solution at each point. They can be calculated by

$$\text{error} = \frac{\sum_{i=1}^{N} \left\| \sigma_i - \sigma_{Hi} \right\|^2}{\sum_{i=1}^{N} \left\| \sigma_{Hi} \right\|^2}, \tag{14}$$

where σ_i is the stress components of LR and SR, and σ_{Hi} is those of HR. In addition, we also calculate a mean square error of the three channels. Table 2 lists the results. The datum in Table 2 indicates that the SR result obtain a closer approaching to the analytical solution. This shows the effectiveness of the proposed super-resolution algorithm to a certain extent.

Table 2. The error analysis of the diametrical loaded disk.

Evaluation object	Project	Principal stress difference	Principal stress sum	Principal stress direction	MSE
Numerical experiment	LR	0.0095	0.0011	0.0020	0.0011
	SR	0.0010	0.00041	0.0011	0.00087
Physical Experiment	LR	0.0113	0.0099	0.0089	0.0107
	SR	0.0020	0.0069	0.0060	0.0050

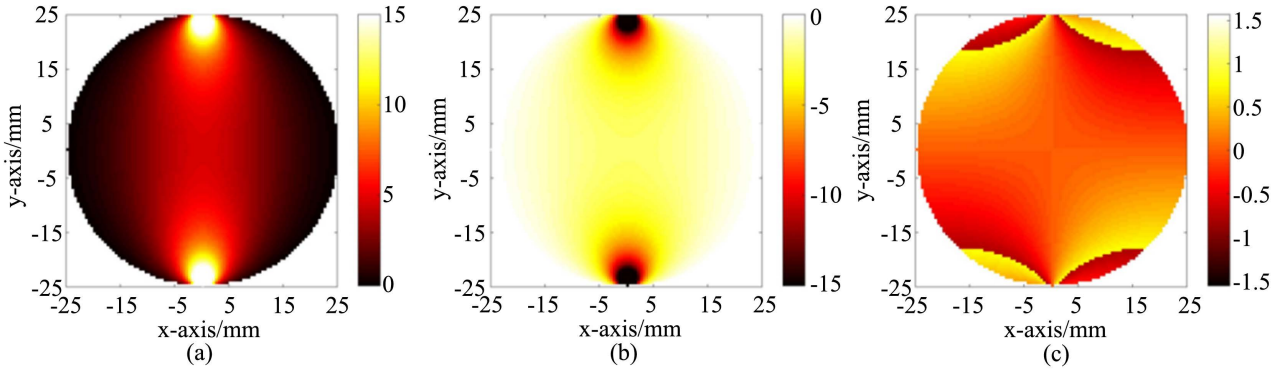

Figure 10. HR stress field (a) the principal stress difference; (b) the principal stress sum; (c) the principal stress direction.

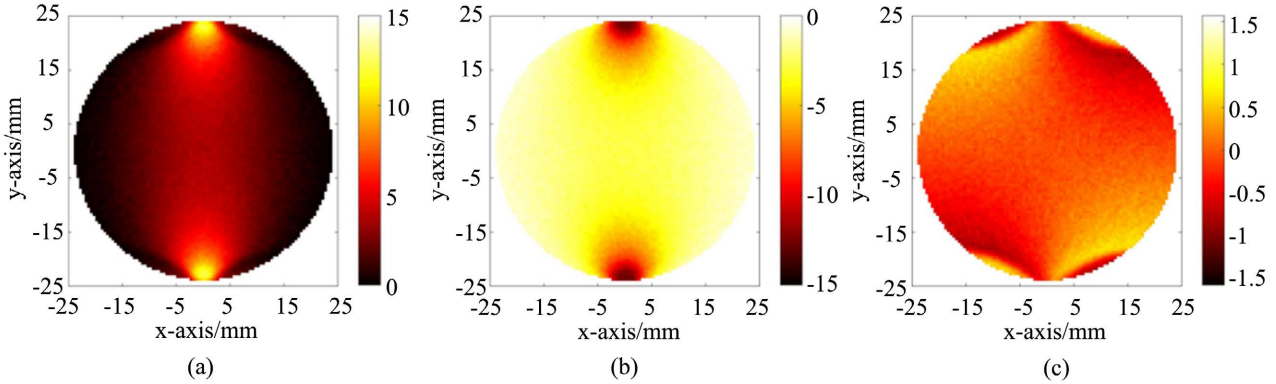

Figure 11. LR stress field (a) the principal stress difference; (b) the principal stress sum; (c) the principal stress direction.

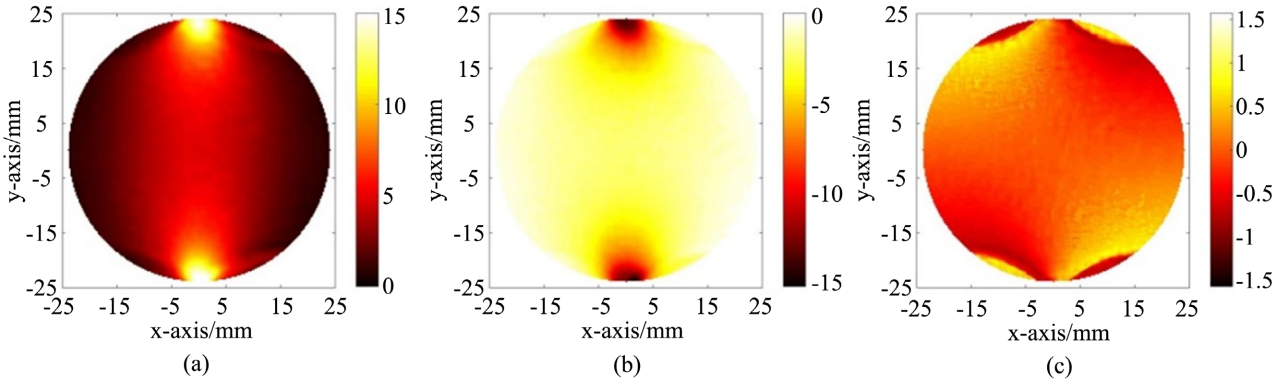

Figure 12. SR stress field (a) the principal stress difference; (b) the principal stress sum; (c) the principal stress direction.

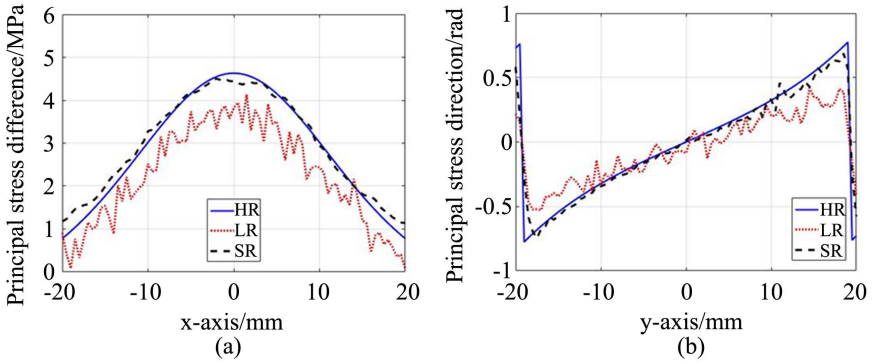

Figure 13. Stress field comparison (a) the principal stress difference when $y = 0$ mm; (b) the principal stress direction when $x = 12.5$ mm.

4. Discussion

In the experiment of diametrical loaded disk, a step of 0.5 mm is used, because the smaller step can measure the stress of each point relatively accurately, which is also the minimum step that can be achieved considering the scanning time. At the same time, 0.5 mm here is the step of low resolution state, that is to say, the pixel of low resolution stress image is 101 × 101. After calculation with the trained network model, the high resolution state step is equivalent to 0.1 mm, that is to say, the pixel of the low resolution stress image is 505 × 505.

In addition, the noise reduction effect of the proposed super-resolution algorithm for stress fields can also save time for the scanning experiment of full-field stress measurement. In order to obtain the terahertz signal with a lower noise level, 50 or 100 times of signal acquisition for each point to be measured is often averaged in the experiment, which causes multiple time loss. The super-resolution algorithm is applied to the measurement experiment, only 20 times of repeated acquisition is needed to take the average value, which greatly saves the time of the experiment.

In this paper, based on the developed SRCNN, we propose an effective super-resolution method for THz stress field imaging using the THz-TDS technology. Based on the Fresnel model, the stress optic effect, and the degradation effect of the used THz-TDS system, a modulation model of plane stress field to the THz-TDS signal is established. By SRCNN algorithm, we train the end-to-end mapping network model of low-resolution stress field to high resolution stress field. A training set of low-resolution stress fields simulated from the established modulation model is used as the input of the network to learn its blur features and noise features. The numerical simulation and physical experiment show that the SRCNN algorithm can partly restore the degradation caused by the large THz spot, limited scanning step and random noise of the used system, improve the resolution of stress distribution image and improve the measurement accuracy. For different imaging systems, the proposed method can be easily applied by estimating the blurred kernel, incorporating it into the training set, and retraining the new model.

Compared with the existing terahertz image super-resolution algorithms, the key difference of the proposed algorithm is that it uses both the amplitude and phase of the THz signal. Since THz radiation can penetrate most non-metallic materials, it is a very potential technology to use THz radiation to image the internal stress field of these optically opaque materials, including some organic Molecule Compounds [23]. The proposed algorithm in this paper can improve the resolution and promote the speed of THz stress imaging, so it can help THz stress imaging obtain more extensive engineering applications.

Funding

This work was supported by the National Natural Science Foundation of China [Grant number 12041201 and 12021002].

Conflicts of Interest

The authors declare no conflicts of interest regarding the publication of this paper.

References

[1] Ferguson, B. and Zhang, X.-C. (2002) Materials for Terahertz Science and Technology. *Nature Materials*, **1**, 26-33. https://doi.org/10.1038/nmat708

[2] Tonouchi, M. (2007) Cutting-Edge Terahertz Technology. *Nature Photonics*, **1**, 97-105. https://doi.org/10.1038/nphoton.2007.3

[3] Stoik, C.D., Bohn, M.J. and Blackshire, J.L. (2008) Nondestructive Evaluation of Aircraft Composites Using Transmissive Terahertz Time Domain Spectroscopy. *Optics Express*, **16**, 17039-17051. https://doi.org/10.1364/OE.16.017039

[4] Mittleman, D.M., Castro-camus, E. and Koch, M. (1999) Recent Advances in Terahertz Imaging. *Applied Physics B*, **68**, 1085-1094. https://doi.org/10.1007/s003400050750

[5] Mittleman, D.M., Hunsche, S., Boivin, L. and Nuss, M.C. (1997) T-Ray Tomography. *Optics Letters*, **22**, 904-906. https://doi.org/10.1364/OL.22.000904

[6] Rutz, F., Hasek, T., Koch, M., Richter, H. and Ewert, U. (2006) Terahertz Birefringence of Liquid Crystal Polymers. *Applied Physics Letters*, **89**, Article ID: 221911. https://doi.org/10.1063/1.2397564

[7] Reid, M. and Fedosejevs, R. (2006) Terahertz Birefringence and Attenuation Properties of Wood and Paper. *Applied Optics*, **45**, 2766-2772. https://doi.org/10.1364/AO.45.002766

[8] Kim, Y., Ahn, J., Kim, B. and Yee, D. (2011) Terahertz Birefringence in Zinc Oxide. *Japanese Journal of Applied Physics*, **50**, Article ID: 030203. https://doi.org/10.1143/JJAP.50.030203

[9] Ebara, S.I., Hirota, Y., Tani, M. and Hangyo, M. (2007) Highly Sensitive Birefringence Measurement in THz Frequency Region and Its Application to Stress Measurement. *Proceedings of Joint* 32*nd International Conference on Infrared and Millimeter Waves and the* 15*th International Conference on Terahertz Electronics*, Cardiff, 2-9 September 2007, 666-667. https://doi.org/10.1109/ICIMW.2007.4516673

[10] Takahashi, T. (2011) Observation of Cavity Interface and Mechanical Stress in

Opaque Material by THz Wave. In: *Behaviour of Electromagnetic Waves in Different Media and Structures*, InTech, Rijeka, 383-398. https://doi.org/10.5772/19670

[11] Li, L.A., Wang, W.S., Wang, Z.Y., Wang, S.B., He, M.X., Han, J.G. and Cong, L.G. (2013) Active Modulation of Refractive Index by Stress in the Terahertz Frequency Range. *Applied Optics*, **52**, 6364-6368. https://doi.org/10.1364/AO.52.006364

[12] Wang, Z. (2016) Determination of Plane Stress State Using Terahertz Time-Domain Spectroscopy. *Scientific Reports*, **6**, Article No. 36308. https://doi.org/10.1038/srep36308

[13] Dong, C., *et al.* (2014) Learning a Deep Convolutional Network for Image Super-Resolution. *European Conference on Computer Vision*, Zurich, 6-12 September 2014, 184-199. https://doi.org/10.1007/978-3-319-10593-2_13

[14] Ledig, C., Theis, L., Huszar, F., Caballero, J., Cunningham, A., Acosta, A. and Aitken, A. (2017) Photo-Realistic Single Image Super-Resolution Using a Generative Adversarial Network. *Proceedings of the* 30*th IEEE/CVF Conference on Computer Vision and Pattern Recognition* (*CVPR*), Honolulu, 21-26 July 2016, 105-114. https://doi.org/10.1109/CVPR.2017.19

[15] Yang, F., Xu, W. and Tian, Y. (2017) Image Super Resolution Using Deep Convolutional Network Based on Topology Aggregation Structure. *AIP Conference Proceedings*, **1864**, Article ID: 020185. https://doi.org/10.1063/1.4993002

[16] Shi, W.Z., Caballero, J., Huszar, F., *et al.* (2016) Real-Time Single Image and Video Super-Resolution Using an Efficient Sub-Pixel Convolutional Neural Network. *Proceedings of the* 2016 *IEEE Conference on Computer Vision and Pattern Recognition* (*CVPR*), Las Vegas, 27-30 June 2016, 1874-1883. https://doi.org/10.1109/CVPR.2016.207

[17] Long, Z., Long, Z.Y., Wang, T.Y., *et al.* (2019) Terahertz Image Super-Resolution Based on a Deep Convolutional Neural Network. *Applied Optics*, **58**, 2731-2735. https://doi.org/10.1364/AO.58.002731

[18] Li, Y.D., Hu, W.D., Zhang, X., *et al.* (2020) Adaptive Terahertz Image Super-Resolution with Adjustable Convolutional Neural Network. *Optics Express*, **28**, 22200-22217. https://doi.org/10.1364/OE.394943

[19] Lu, Y., Mao, Q. and Liu, J.B. (2021) Mathematical Degradation Model Learning for Terahertz Image Super-Resolution. *IEEE Access*, **9**, 128988-128995. https://doi.org/10.1109/ACCESS.2021.3113258

[20] Ljubenovic, M., Bazrafkan, S., Paramonov, P., De Beenhouwer, J. and Sijbers, J. (2020) CNN-Based Deblurring of THz Time-Domain Images. 15*th International Joint Conference*, *VISIGRAPP* 2020, Valletta, 27-29 February 2020, 477-494. https://doi.org/10.5220/0008973103230330

[21] Ljubenović, M., Artesani, A., Bonetti, S. and Traviglia, A. (2022) Beam-Shape Effects and Noise Removal from THz Time-Domain Images in Reflection Geometry in the 0.25-6 THz Range. *IEEE Transactions on Terahertz Science and Technology*, **12**, 574-586. https://doi.org/10.1109/TTHZ.2022.3196191

[22] Jia, Y.Q., Evan, S., Jeff, D., *et al.* (2014) Caffe: Convolutional Architecture for Fast Feature Embedding. 22*nd ACM International Conference on Multimedia*, Orlando, 3-7 November 2014, 675-678. https://doi.org/10.1145/2647868.2654889

[23] Bibelayi, D., Lundemba, A., Tsalu, P., Kilunga, P., Tshishimbi, J. and Yav, Z. (2022) Hydrogen Bonds of C = S, C = Se and C = Te with C-H in Small-Organic Molecule Compounds Derived from the Cambridge Structural Database (CSD). *Crystal Structure Theory and Applications*, **11**, 1-22. https://doi.org/10.4236/csta.2022.111001